IEEE Access
Multidisciplinary ⋮ Rapid Review ⋮ Open Access Journal

Received 11 February 2026, accepted 16 March 2026, date of publication 31 March 2026, date of current version 7 April 2026.

Digital Object Identifier 10.1109/ACCESS.2026.3679616

RESEARCH ARTICLE

A Three-Layer AI-Driven Image Filtering for Efficient LEO Satellite Remote Sensing

NOURHEN SBOUI[1], (Student Member, IEEE), HAKIM GHAZZAI[2], (Senior Member, IEEE), SAMEH NAJEH[1], (Member, IEEE), AND LOKMAN SBOUI[3], (Senior Member, IEEE)

[1]Higher School of Communications of Tunis (SUP'COM), University of Carthage, Tunis 1054, Tunisia
[2]King Abdullah University of Science and Technology (KAUST), Thuwal 23955, Saudi Arabia
[3]École de Technologie Supérieure (ÉTS), University of Québec, Montreal, QC H3C 1K3, Canada

Corresponding author: Hakim Ghazzai (hakim.ghazzai@kaust.edu.sa)

This work was supported by the Natural Sciences and Engineering Research Council of Canada (NSERC) Discovery Grant, "Satellite Connectivity and AI-Based Data Management of Time-Critical IoT Applications in Remote Areas," under Grant RGPIN-2024-06584.

ABSTRACT Low-earth orbit (LEO) satellites are considered essential tools for remote sensing (RS) and Earth observation (EO) applications thanks to their high spatial resolution images. However, limited on-board resources (storage, downlink throughput, and bandwidth) make it challenging to manage the large volume of data collected. Real-time data management is needed to avoid wasting on-board compute and downlink budget, especially when dealing with a significant influx of anomalous data images resulting from factors such as redundancy, seasonal changes, sensor properties, and satellite orbit dynamics. This paper introduces a novel three-layer filtering solution designed to optimize satellite image transmission for EO. Incorporating a fusion of machine learning and deep learning methodologies, our data management solution mitigates critical challenges associated with LEO satellite resource constraints. The proposed solution includes a no-reference deep image quality assessment (NoR-DIQA) model using a convolutional neural network architecture to identify and filter out distorted images. Then, it employs a perceptual hashing redundancy detection approach to eliminate duplicated images, and finally, it employs a classification model that categorizes suitable RS and EO applications for each image set before transmission. This framework effectively maximizes data utility and optimizes resource allocation for RS and EO satellites. The proposed framework was tested on different RS and EO datasets, where each layer was benchmarked against established models and consistently achieved superior results (e.g., higher correlation and lower error in image quality assessment, improved redundancy detection, and classification accuracy up to 99.4%), demonstrating the robustness and reliability of the three-layer filtering solution.

INDEX TERMS Earth observation, remote sensing, deep image quality assessment, classification, LEO image filtering.

I. INTRODUCTION

Our world is experiencing an unprecedented digital transformation, marked by the prolific collection of vast amounts of data, where low-earth orbit (LEO) satellites are playing a pivotal role as sensing platforms [1]. Positioned at low altitudes, LEO satellites enable reduced communication latency, near-real-time data transmission, and frequent revisits to the same Earth locations. They offer advantages such as low cost, data freshness, and efficient spectrum allocation [2], making them crucial for remote sensing (RS) and Earth observation (EO) applications such as urban planning, agriculture, disaster monitoring, and environmental surveillance [3], [4], [5], [6], [7]. However, these satellites face challenges, including limited resources, bandwidth, and budgets. Their rapid orbits result in short communication windows, restricting data collection and transmission opportunities, particularly for applications requiring continuous data flow. Additionally, bandwidth limitations hinder the volume and speed of data transfer [8].

Moreover, since LEO satellites rely on solar power as their primary energy source, they are vulnerable to distribution challenges caused by atmospheric changes, which can affect data management and transmission reliability, leading to

The associate editor coordinating the review of this manuscript and approving it for publication was Manuel Rosa-Zurera.

potential delays or interruptions. Additionally, their compact size and limited weight limit onboard data storage capacity, making it difficult to collect, process, and transmit large data volumes to ground stations and EO applications [9]. The high volume of outliers, anomalies, and redundancies in LEO images further contributes to these challenges, as these low-value images increase data volume, consume on-board resources and power, and increase delivery cost. Addressing these data-related challenges involves minimizing image delivery, eliminating redundancies, filtering distorted data, and categorizing images based on their intended use [10]. Such an approach is crucial for overcoming budget constraints, time-efficient transmission, bandwidth limitations, storage capacity issues, and energy constraints.

To address resource constraints in the remote sensing field, numerous research studies have been proposed in the literature. For instance, in [11], the authors introduced a spatial resampling of RS data to assess whether the use of high-resolution data in the analysis of vegetation in an intensively used meadow with a homogeneous cover is advisable or whether it generates a large amount of redundant information, which aims to reduce the costs of retrieval of data for various purposes in the future. Moreover, in [12], a reduction technique for hyperspectral RS image classification is proposed using multiple PCA-based approaches, such as PCA, SPCA (Segmented-PCA), and SSPCA (Spectrally Segmented-PCA), to enhance classification performance. These band-reduction strategies can be categorized into feature-extraction and feature-selection methods.

Complementary efforts have also focused on network-level optimization for satellite data transport. For example, in [13], a multi-hop coflow scheduling process in LEO satellite networks was formulated as a routing and bandwidth allocation problem, with the proposed Coflow Routing Greedy Scheduling (CRGS) algorithm mitigating bandwidth contention in multi-hop links. A dynamic data routing for LEO satellite–based communications was modeled to evaluate reliability and efficiency improvements in the network [14]. In parallel, AI-driven decision support systems have been investigated to enhance data transport efficiency [15]. A decentralized satellite-federated learning framework was proposed in [16] to address single-point failures and slow convergence caused by intermittent communication, while also considering traffic limitations, data privacy, and machine learning efficiency.

Another line of research has emphasized the use of on-board AI for image compression and data reduction. In particular, the Φ-Sat-2 mission demonstrated the feasibility of applying a convolutional autoencoder-based lossy compression algorithm directly on CubeSats [17]. This approach reduces bandwidth usage and storage demands by performing intelligent compression in orbit. Similarly, simulation frameworks for multispectral and hyperspectral products have been developed to support the design of on-board machine learning applications, enabling realistic benchmarking and training of EO algorithms in representative orbital environments [18]. A recent review of edge AI for EO [19] has also summarized emerging techniques such as lightweight model design, pruning, quantization, and federated learning, all tailored for resource-constrained space systems. These studies highlight the growing interest in shifting intelligent processing closer to the data source.

Despite these advances, existing solutions primarily focus on data compression or transmission efficiency, without addressing the problem of transmitting low-quality, redundant, or irrelevant images. In such cases, even highly compressed data still represents wasted bandwidth, storage, and energy. Therefore, a critical research gap remains: the absence of a comprehensive framework that not only compresses and transmits data efficiently but also intelligently filters images by quality, redundancy, and relevance before transmission.

In this study, we aim to develop a novel solution, the three-layer image filtering framework, to address the fundamental challenge of efficient data management for LEO satellite, where vast amounts of imagery are often degraded by distortions, duplicated due to frequent revisits, or irrelevant to mission objectives. These issues waste limited onboard resources, increase transmission delays, and elevate operational costs. To tackle these challenges, the proposed three-layer image filtering framework optimizes the quality and relevance of collected satellite images before transmission. The first layer employs a no-reference deep image quality assessment (NoR-DIQA) model to identify and discard distorted images using a CNN trained with artificial mean opinion scores (AMOS). The second layer removes redundant data through perceptual hashing, while the third layer classifies the remaining images according to their targeted RS and EO applications, discarding non-relevant content. Through this hybrid framework, we aim to minimize bandwidth usage, reduce storage and transmission burdens, and maximize the utility of downlinked imagery. We validate the proposed approach on multiple RS and EO datasets and benchmark it against baseline models to demonstrate its effectiveness. The contributions of this paper can be summarized as follows:

- We investigate the problem of data management on LEO satellites for RS and EO applications by proposing an AI-driven framework that autonomously eliminates low-quality, redundant, and irrelevant data. The framework is designed as a three-layer pipeline to reduce the volume of data transmitted to ground stations and alleviate congestion over low-bandwidth LEO communication links.
- We adapt a no-reference deep image quality assessment (NoR-DIQA) model for LEO satellite images to identify and filter out distorted data. The model leverages the feature extraction capability of a lightweight CNN architecture, trained using an artificial mean opinion score (AMOS) labeling process derived from objective perceptual quality metrics.

- We implement a redundancy removal method combined with an EO classification technique to efficiently discard duplicate and irrelevant images. Redundancy is detected using a perceptual hashing (PH) algorithm, while a deep learning classifier categorizes the remaining images according to their RS and EO applications.

In summary, the outcome of this work is the development of an integrated three-layer filtering framework that significantly improves the efficiency of LEO satellite image transmission by ensuring that only high-quality, non-redundant, and application-relevant data are retained. To validate the effectiveness of the proposed approach, we conducted extensive experiments on benchmark RS and EO datasets, incorporating multiple types of distortions that mimic real LEO conditions. The fine-tuned NoR-DIQA model was evaluated against traditional full-reference and no-reference image quality assessment methods, showing superior correlation with perceptual quality scores. The redundancy removal step was validated using a perceptual hashing with different thresholds. Finally, the classification layer was assessed using two pre-trained deep learning architectures, Wide ResNet-50 and VGG-16, highlighting strong generalization performance and clear advantages over baseline models. The end-to-end framework is then evaluated and tested to confirm that it not only addresses the fundamental challenges of data congestion in LEO satellites but also provides a scalable and reliable solution for real-world EO and RS applications.

The remainder of this paper is organized as follows. Section II presents the architecture of the proposed AI-driven satellite imagery management framework. Section III delves into the different components of the proposed framework and describes the algorithms for quality assessment, image redundancy elimination, and image classification. Section IV presents the simulation results. Finally, Section V concludes the paper.

II. THREE-LAYER FILTERING FRAMEWORK FOR EO IMAGES

LEO satellite images face various challenges, including inaccuracies caused by satellite orbit, atmospheric conditions, and sensor properties, which affect image quality and utility. Seasonal changes, compression, and other factors contribute to redundant data, increasing the volume of LEO data and consuming satellite resources such as computational power, bandwidth, and energy. Despite these challenges, the importance of RSI for RS and EO applications underscores the need for high-quality, relevant data. To address these issues, a three-layer filtering framework is proposed for integration directly into LEO satellites. This framework filters redundant images, retaining only essential and relevant data by excluding low-quality, duplicated, and irrelevant images. The remaining images are categorized based on their intended RS and EO applications. This approach effectively addresses the challenges posed by limited LEO satellite resources while managing large data volumes. In the following, we first introduce the workflow of the proposed three-layer image filtering framework for satellite image optimization (see Figure 1), followed by a description of the dataset used in this work.

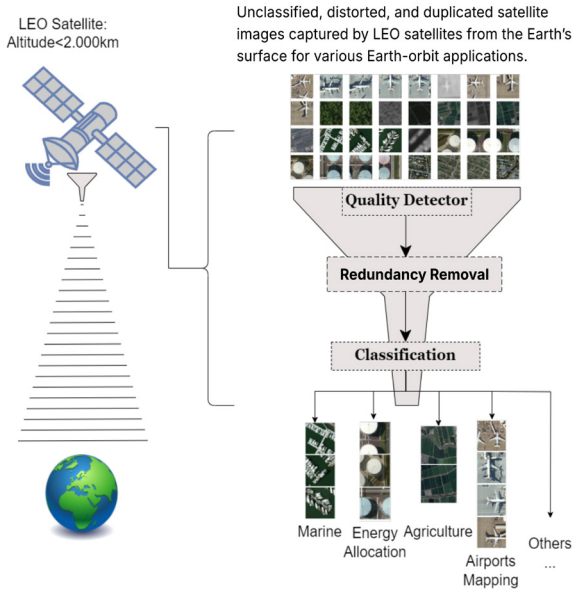

FIGURE 1. Three-layer image filtering framework to discard anomalous LEO satellite images.

A. THREE-LAYER FILTERING FRAMEWORK

The initial layer of our proposed solution involves a real-time assessment of the quality and utility of the LEO satellite image. This assessment, using a fast, automated approach, predicts image quality without requiring a reference image. We aim to filter out low-quality images and thereby minimize the size of the LEO satellite dataset. Taking advantage of the strong representational power of CNNs, we propose a deep learning algorithm for NR-IQA. Unlike traditional methods, our model does not rely on an original image, making it specific to LEO satellite imagery. This approach aims to better reflect human perceptual judgment, consistent with the objective of natural-image IQA models. Due to the scarcity of RSI, especially LEO satellite images, traditional collection methods are time-consuming. To address this, we propose a labeling methodology that adds random distortions to a real-world LEO satellite dataset. These distorted images, along with their clean versions, form an AMOS used to train the NoR-DIQA model, considering scenarios unique to RSI cases.

The second layer of our proposed framework focuses on redundancy elimination, aiming to discard similar LEO satellite images and optimize data transfer efficiency. LEO satellites often capture multiple frames of the same location with minor or static changes, leading to redundancy. To address this, we employ perceptual hash (PH) methods

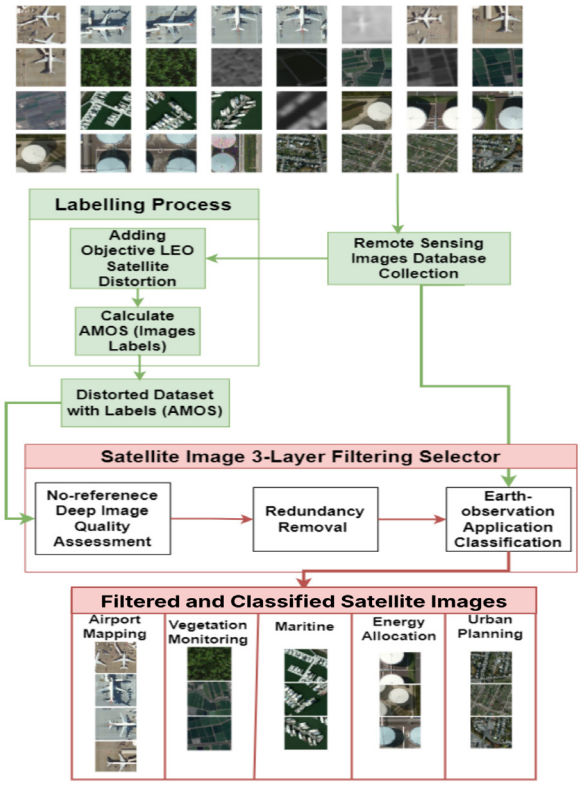

FIGURE 2. Detailed three-layer image filtering framework workflow.

from a validated family [20] that has undergone extensive testing on various open image databases [21], particularly in RSI scenarios with different alterations and noises. PH algorithms excel at content-based authentication, accounting for crucial properties of LEO imagery, such as structures and resolution. Specifically, edge-feature-based perceptual hash algorithms achieve superior tampering-authentication accuracy for high-resolution RSI (HRRSI) imagery compared to standard techniques.

The third and final layer is dedicated to RS and EO application classification. Inspired by the exceptional performance of pre-trained deep learning models in natural image classification, we propose using a deep learning model to classify LEO satellite images for RS and EO applications. An additional class is introduced to classify images that do not belong to any specific application, leading to their exclusion. Our study conducts a comparative RS and EO classification analysis using a highly scalable and categorized database with high spatial resolution. We evaluate two pre-trained deep learning architectures, namely ResNet and the Visual Geometry Group (VGG), for this classification task.

In Figure 2, we present a detailed workflow of the three-layer image filtering selector framework tailored for LEO satellite images. The architecture involves distinct phases depicted by green lines, representing the training process, and a red line indicating the inference process. Furthermore, we demonstrate the framework's application using RSI as input. The resulting output comprises classified, relevant data images without redundancy, showcasing its potential utility in satellite image processing.

B. EO IMAGE DATASET AND PREPROCESSING

1) DATASET DESCRIPTION

The framework performance is significantly impacted by the size of the database. In the context of EO, a large, diverse dataset is crucial. High spatial resolution is also essential for effective learning and generalization in deep learning models. However, databases such as LEO satellite image datasets for RS and EO application classification are currently limited compared to typical computer vision and deep learning datasets. Addressing the limitations of IQA models based on natural images, especially with the impact of data augmentation on perceptual and technical quality scores, presents challenges in incorporating human subjective labels for satellite images. To overcome this issue, we propose using the RSI classification benchmark RSI-CB256 [22] for training, testing, and validation datasets in both layers 1 and 3.

The RSI-CB256 dataset comprises 24,740 images with a 256 × 256 pixel size in TIFF format [22]. It contains more than 24,000 images across 35 categories, with approximately 690 images per category. This benchmark has a higher spatial resolution than other existing databases (0.22–0.3 m), which can also be clearly observed from the larger image memory size. The dataset is organized into six main categories: agricultural land, construction land and facilities, transportation and facilities, water and water-conservancy facilities, forest, and other lands. Each category is further divided into several sub-classes, with their corresponding image counts presented in Figure 3, along with some examples of RSI-CB256 images illustrated in Figure 4. This dataset has demonstrated strong performance in training CNN models compared with other satellite datasets, such as UC-Merced [23], a well-known benchmark for scene classification. Similarly, SAT-4 and SAT-6 [24] are two other important benchmarks widely used in RSI classification studies. Recently, a satellite image classification model was proposed in [25], demonstrating that RSI-CB256 is well-suited for both fine-grained and global feature extraction. The same dataset has also been employed in studies addressing data imbalance and long-tailed distributions in RS, such as the diffusion-noise-based augmentation framework proposed in [26], which leverages generative models to improve class diversity and robustness. Motivated by its widespread adoption and demonstrated effectiveness in prior studies, RSI-CB256 was selected as a representative benchmark for validating the proposed three-layer filtering framework.

2) DISTORTION INJECTION

Distortions in LEO satellite imagery arise from factors such as orbit dynamics, atmospheric conditions, temporal

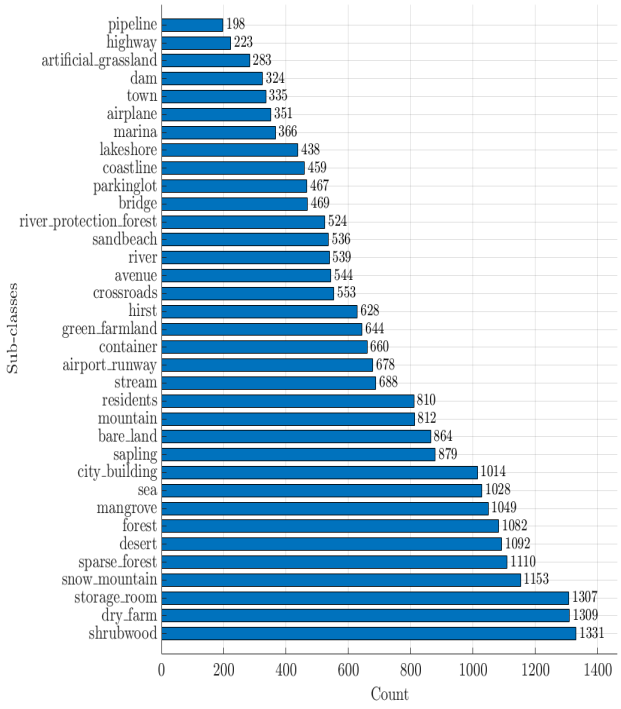

FIGURE 3. Number of images per sub-class in RSI-CB256.

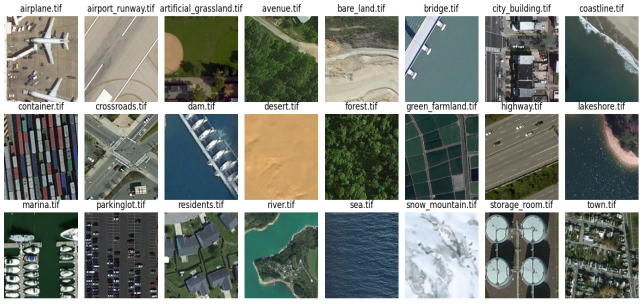

FIGURE 4. RSI-CB256 original images.

variations, and sensor alignment issues, thereby affecting resolution, quality, and accuracy. Atmospheric interference, sun angle, temperature inversions, and scattering from clouds, haze, and dust degrade visual contrast, blur images, and affect color accuracy. Temporal and terrain variations, along with Earth's curvature and elevation changes, introduce radiometric and geometric inaccuracies. These real-world factors were key to introducing distortions into the RSI-CB256 database, reflecting the challenges LEO satellite images face across various scenarios. Therefore, in this study, we propose adding more distortions to the RSI-CB256 database to reflect the natural effects of real-world conditions to which LEO satellite images can be subjected due to the previously mentioned factors. The types of distortions employed in this work are:

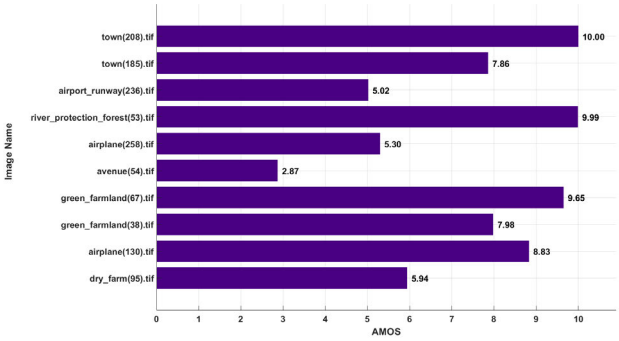

FIGURE 5. AMOS output results related to previous RSI-CB256 testing images.

- **Blur distortion:** Satellite speed, atmospheric turbulence, sensor properties, and environmental conditions contribute to image distortion. When combined, these factors reduce visual sharpness and detail, resulting in lower image clarity.
- **Lens flare:** Lens flare, a type of light streak, can be created by unwanted sources like the sun, artificial light, or camera sensor coatings and design.
- **Radiometric distortion:** This distortion refers to the variation in the intensity of light or the values of the pixels throughout the image that affects the accuracy and reliability of the data.
- **Quantization noise:** These inaccuracies occur when continuously varying analog data (such as the brightness or radiometric values of an image) are quantified.
- **Temporal noise:** refers to variations in image quality and accuracy caused by factors that affect satellite sensors or data collection processes at different times.
- **Striping noise:** Characterized by the presence of visible bands or streaks of varying brightness or color, which frequently appear as regular patterns or lines.

These various distortions were randomly introduced into the RSI-CB256 images using random noise factors. To ensure harmonized distorted images, we retain some images without distortion and randomly vary the noise factors across their lowest and medium values to better simulate real-world scenarios. In Figure 6, we display examples of altered images (i.e., originals in Figure 4) along with their corresponding applied distortions.

III. AI-DRIVEN TECHNIQUES FOR RSI MANAGEMENT

In this section, we present in detail the three layers of the proposed framework.

A. LAYER 1: NO-REFERENCE DEEP IQA FOR LEO SATELLITE IMAGES OPTIMIZATION

Traditional methods for IQA focus on predicting subjective quality scores to align with human perceptual judgment. However, metrics such as mean square error (MSE) [27], and peak signal-to-noise ratio (PSNR) [28] struggle to accurately replicate the human visual system. Similarly, the visual

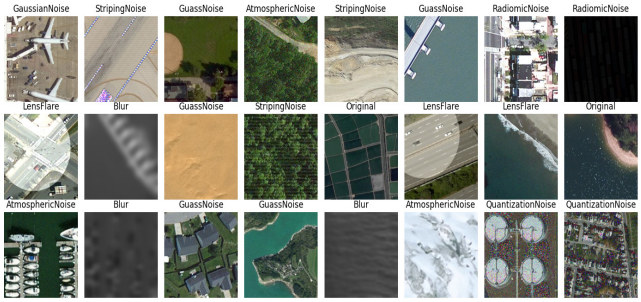

FIGURE 6. RSI-CB256 images after being distorted randomly. The type of distortion is indicated at the top of each image.

information fidelity criterion (VIF) [29] faces challenges with complex textures and patterns in LEO satellite images and is sensitive to variations in spatial resolution and dynamic scenes. Additionally, the structural similarity index (SSIM) [30] and feature similarity index (FSIM) [31] are highly sensitive to scale changes, details, and large-scale structures, making them less effective for multi-resolution or diverse-scale remote sensing images (RSI).

A significant challenge in IQA is measuring distortion relative to an ideal imaging model or reference image. Full-Reference (FR) IQA methods work well when reference images are available, directly comparing distorted and ideal versions. However, in cases without reference images, no-reference (NR) IQA methods are crucial, relying on discriminant features often based on natural scene statistics (NSS) [32]. While NSS may not fully align with the characteristics of RSI, traditional methods that use computationally intensive transformations, such as wavelets or DCTs, are common. Recent methods, such as CORNIA [33] and BRISQUE [34], use spatial-domain features, reducing computational time and effectively addressing the complex textures and patterns in RSI.

Based on these observations, we propose using a CNN for NR-IQA, enabling autonomous learning of discriminative features directly from raw images. Unlike traditional methods that rely on handcrafted features, this approach learns features from normalized raw image pixels, resulting in superior performance. This is especially effective for local evaluation of LEO satellite images. Traditional IQA models struggle with the multifaceted distortions inherent in the data, highlighting the need for a more adaptive solution. Deep learning IQA models based on CNNs are ideal for addressing these challenges, as they learn features adaptively from large datasets. This adaptability ensures a more accurate and contextually relevant evaluation of image quality within the LEO satellite domain.

1) ARTIFICIAL MEAN OPINION SCORE FOR IMAGE QUALITY ANNOTATION

To ensure robust alignment between the proposed Artificial Mean Opinion Score (AMOS) and human subjective evaluations, we introduce a reference-based quality metric that combines the Multi-Scale Structural Similarity Index (MS-SSIM) and the Learned Perceptual Image Patch Similarity (LPIPS) with a VGG16 backbone. These metrics are selected due to their well-documented alignment with human perception and their ability to quantify structural and perceptual distortions commonly encountered in LEO satellite imagery.

MS-SSIM, an extension of the traditional structural similarity index (SSIM), offers enhanced robustness and accuracy, especially for distorted images. Considering structural information at multiple scales, MS-SSIM is well-suited for evaluating image quality, which is crucial for LEO satellite images with diverse distortions. Its values range from 0 (complete dissimilarity between the reference and altered images) to 1 (complete similarity between the two).

Similarly, the **LPIPSvgg16** index, a deep learning-based perceptual similarity metric, employs features extracted from a pre-trained VGG16 network to measure perceptual differences between images. Unlike traditional metrics, LPIPSvgg16 aligns with human visual perception by capturing subtle degradations such as blurring, noise, and compression artifacts. Its values also range from 0 (perceptually identical to the reference) to 1 (maximally dissimilar).

To unify these complementary perspectives, we fuse MS-SSIM and LPIPSvgg16 into the AMOS metric. Since both components require a reference image, AMOS is inherently a reference-based metric. The fused score compensates for individual limitations: MS-SSIM emphasizes structural fidelity, while LPIPSvgg16 addresses perceptual degradations. To align with the conventional 0–10 MOS scale used in human evaluations, we normalize and rescale the combined score as follows:

$$AMOS = 10\left(\frac{\text{MS\_SSIM} + (1 - \text{LPIPSvgg})}{2}\right), \quad (1)$$

where 0 corresponds to severe distortion (low quality), and 10 indicates perfect similarity to the reference (high quality).

Figure 5 illustrates the final output in the form of AMOS, mimicking the human subjective quality assessment of these altered images in comparison to their pristine versions.

It is important to note that the AMOS used to train the NoR-DIQA model is derived from a fusion of MS-SSIM and LPIPS rather than from genuine human subjective evaluations. As such, this labeling strategy can be considered pseudo-labeling and may introduce bias toward the perceptual characteristics captured by these metrics. Consequently, the proposed NoR-DIQA model may partially learn a surrogate representation of MS-SSIM/LPIPS rather than fully modeling human perceptual quality. Nevertheless, this choice is motivated by the lack of large-scale subjective quality annotations for remote sensing imagery and the practical difficulty of collecting MOS for satellite data. Importantly, the model operates in a fully no-reference manner at inference time and demonstrates strong correlation with perceptual quality indicators across diverse distortions. In a future and more elaborate work, the integration of subjective

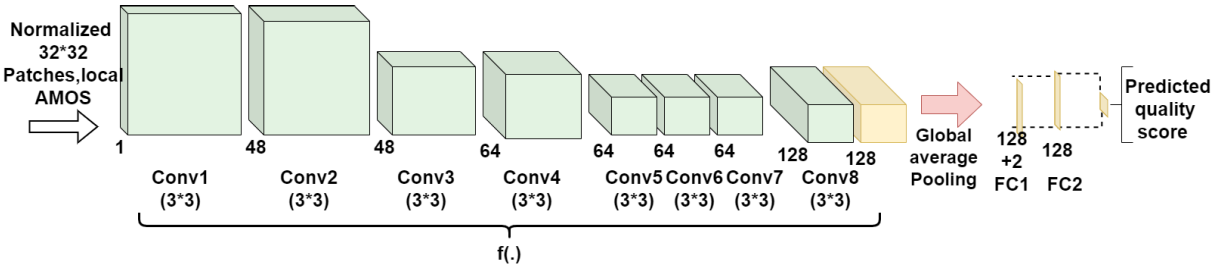

FIGURE 7. No-reference image quality assessment (NoR-DIQA) model architecture.

annotations, human-in-the-loop evaluation, or hybrid labeling strategies will be investigated.

2) NoR-DIQA NETWORK ARCHITECTURE

As presented in Figure 7, the proposed deep CNN model design for assessing the quality of LEO satellite images without the presence of reference images consists of a locally normalized 32×32 image patch input to 8 2D convolutional layers with a kernel size of 3×3. The stride is set to 1 for all convolutional layers except the second and fourth layers; the stride is 2, and one padding for the first 7 2D convolutional layers is set to 0 in the final convolutional layer. All the previous 8 2D-convolutional layers use the ReLU activation function. After that, two fully connected layers, Fc1 with 128 units and ReLU activation, and Fc2 with 1 unit, will map the output of the previous convolutional layers to a 128-dimensional space and then to a one-dimensional space.

3) TRAINING

In dataset preparation, prior work processes images by converting RGB TIFFs to grayscale for simplicity and computational efficiency. These grayscale images are transformed into PILL objects for easier processing and are divided into 32×32-pixel patches, which are locally normalized during training. Each patch is assigned an AMOS as the ground truth for predicting local image quality. The ADAM optimizer is used, with a learning rate of 9×10^{-5} and a weight decay of 10^{-4}. The training loop employs forward and backward passes to adjust the model, with the loss function (lossFunc) quantifying the difference between predicted quality scores and AMOS. It is given as follows:

$$\text{lossFunc} = \frac{1}{n} \sum_{i=0}^{n-1} \text{lossFunc}_i, \tag{2}$$

where

$$\text{lossFunc}_i = \left| f(x_{n,i}, \text{AMOS}_{n,i}) - q_i \right|, \tag{3}$$

is the loss function of each 32-pixel patch at the i^{th} patch, n is the number of patches in a single image, q_i is the local predicted quality of the i^{th} patch, $\text{AMOS}_{n,i}$ is the i^{th} AMOS that is correlated with the i^{th} patch, $x_{n,i}$ is the 32-pixel patch of the input image, and $f(.)$ presents the input function of $x_{n,i}$ and $\text{AMOS}_{n,i}$.

After completing the training, the model's performance on the test dataset is evaluated. Many quality assessment metrics will be computed and analyzed in Section IV to shed light on the model's capacity to predict image quality.

B. LAYER 2: REDUNDANCY REMOVAL

This subsection introduces the second layer of the image filtering framework, focusing on PH-based redundancy detection and removal. Redundancy in LEO satellite imagery, caused by factors such as temporal swathing, compression, data backup, and weather conditions, wastes computational resources, increases power consumption, raises costs, and extends transmission times, especially in bandwidth-limited scenarios. This inefficiency in data retrieval can lead to longer wait times for users querying satellite imagery datasets. To address these issues, we present the PH redundancy detection approach as the second layer in our satellite image filtering framework. This simple technique aims to mitigate drawbacks, maximize data utility, and optimize resource allocation within the EO satellite dataset.

Perceptual image hashing generates content-based image hashes that identify duplicate images by measuring the similarity between them. In dealing with vast EO satellite imagery datasets prone to various distortions, PH is the optimal choice. PH is designed to resist common image distortions, enabling it to match and recover images despite distortions in LEO satellite imagery during transmission and processing. Its computational efficiency, compared to raw-pixel comparisons, is crucial for processing large volumes of satellite images, reducing the resources required for interpretation and retrieval. Moreover, PH scales efficiently for big datasets, making it suitable for both archived and real-time data from multiple LEO satellites.

This method begins by extracting distinguishing features from input images, normalizing them to mitigate differences, and creating a compact representation to capture key perceptual information. Quantization then reduces susceptibility to slight variations. Our proposed redundancy removal method converts images to grayscale, computes perceptual hashes, and identifies redundancy using the Hamming distance between these hashes, offering an efficient, distortion-resistant approach. In this context, we can modularize the process to compute PH for redundancy detection with the following steps:

1) **Convert Images to Grayscale and Resize:** First, we convert the image I to grayscale, reducing the color dimensions and resizing it to a smaller fixed dimension, typically 8×8 pixels, to reduce computational complexity and focus on essential details as follows:

$$I_{\text{gray}} = \text{Grayscale}(I), \quad I_{\text{resized}} = \text{Resize}(I_{\text{gray}}, (8, 8)). \tag{4}$$

2) **Apply Discrete Cosine Transform (DCT):** Then, we apply the 2D Discrete Cosine Transform (DCT) to the resized grayscale image to transform it into the frequency domain, keeping only the most significant low frequencies (top-left of the transformed matrix) as follows:

$$I_{\text{dct}} = \text{DCT}(I_{\text{resized}}). \tag{5}$$

3) **Select Low Frequencies:** From I_{dct}, we select a subset of low-frequency components (e.g., the top-left 8×8 block), as these represent the most prominent image features as follows:

$$I_{\text{low\_freq}} = I_{\text{dct}}[:8, :8]. \tag{6}$$

4) **Compute Average DCT Value:** We calculate the mean of the DCT values (excluding the DC component or $I_{\text{low\_freq}}[0, 0]$) and then create a binary hash by comparing each element in $I_{\text{low\_freq}}$ with the average μ as follows:

$$\mu = \frac{1}{N}\sum_{i=1}^{N} I_{\text{low\_freq}}[I], \; h_i = \begin{cases} 1 & \text{if } I_{\text{low\_freq}}[i] \geq \mu, \\ 0 & \text{otherwise,} \end{cases} \tag{7}$$

where N is the number of elements in $I_{\text{low\_freq}}$. Then, we concatenate the bits h_i to form the final perceptual hash. Using the above steps, the PH (PH) for an image I, which can be expressed as:

$$PH = \text{concat}\left(\left\{h_i = \begin{cases} 1 & \text{if } I_{\text{low\_freq}}[i] \geq \mu \\ 0 & \text{otherwise} \end{cases}\right\}_{i=1}^{N}\right), \tag{8}$$

where $I_{\text{low\_freq}}$ is the set of low-frequency DCT coefficients,μ is the mean of the DCT coefficients, and h_i are the binary hash bits.

Finally, to detect redundancy between two images A and B, we calculate the Hamming distance d between their perceptual hashes PH_A and PH_B as follows:

$$d(H_A, H_B) = \sum_{j=1}^{N} |H_A[j] - H_B[j]|. \tag{9}$$

If d is below a predefined threshold T, the images are considered similar to each other, and one of them can be discarded.

C. LAYER 3: RS AND EO APPLICATION CLASSIFIER

The third layer of the filtering framework focuses on satellite RS and EO image classification, which is essential for optimizing the use of satellite imagery. Classification is vital for various RS and EO applications, such as environmental monitoring and national security, and helps allocate limited satellite resources efficiently. It supports policymakers in prioritizing needs, reducing costs, and ensuring data is collected and transmitted effectively for specific purposes. This layer also addresses challenges related to diverse data volumes and resolutions while prioritizing data transmission under bandwidth constraints. Recent advancements in pre-trained deep CNNs, inspired by their success on the ImageNet dataset [35], [36], have shown promise for RSI classification. Training deep CNNs on a large-scale dataset such as RSI-CB256 ensures better generalization, prevents overfitting, and enhances model accuracy. This approach optimizes data utility, storage, bandwidth, and costs. The section will detail two investigated pre-trained CNN-based classification systems, specifically Wide ResNet-50-2 and VGG16. The training parameters of the Wide ResNet-50-2 and VGG16, as well as their optimized hyperparameters, are given in Tables 1 and 2.

1) WIDE ResNet-50-2

The DCNN RS and EO classification pipeline, based on a pretrained Wide ResNet-50-2 [37], commences with image preprocessing, during which 256×256 images are resized to 64×64 per batch. Subsequently, these modified images are partitioned into three distinct datasets: training, testing, and validation. The choice of network architecture stems from its remarkable performance on ImageNet. Specifically, a pre-trained Wide ResNet-50-2 is employed for feature extraction, with its layers held fixed (frozen) during training. The output from the pre-trained layers is then channeled through a custom, fully connected head architecture designed to address our classification task. This specialized head architecture consists of a linear layer with 256 outputs, followed by a ReLU activation, which introduces essential non-linearity to the model. To guard against overfitting, a dropout layer with a dropout rate of 0.5 is thoughtfully integrated. Finally, a fully connected layer with 35 outputs, matching the number of RSI-CB256 classes, produces class logits. To facilitate training, a LogSoftmax layer is appended to the classification network's final output. This transformation converts class logits into log-probabilities, which are instrumental for computing the cross-entropy loss during training.

2) VGG16

The architecture and design of this model are rooted in VGG16 [38], tailored for multiclass classification. To train the RS and EO classification model, the model leverages pretrained VGG16 layers for feature extraction. The features extracted from these layers are subsequently fed into a sequence of fully connected layers with 256 input nodes and

TABLE 1. Training parameters of the pre-trained classification models for RS and EO applications.

Training Parameters	Wide ResNet-50	VGG-16
Loss Function	Cross-entropy loss	Cross-entropy loss
Optimizer	ADAM	ADAM
Learning Rate	Learning Rate Scheduling	Learning Rate Scheduling
Regularization	Dropout with a dropout rate of 0.5	Dropout with a dropout rate of 0.5
Early Stopping	3 epochs	3 epochs

TABLE 2. Hyperparameter optimization of the Wide ResNet-50-2 and VGG-16.

Hyperparameters	Wide ResNet-50-2	VGG-16
The number of training epochs	**20**	**20**
The maximum learning rate	0.0001	0.0001
Gradient clipping	0.1	0.1
Weight decay	0.001	0.001
The batch size	64	64

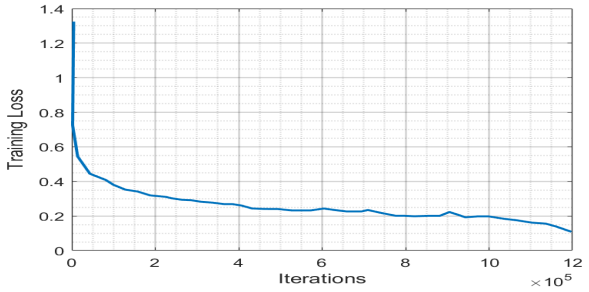

FIGURE 8. Training Loss Function measures of the Deep No-reference IQA model during 500 epochs on RSI-CB256.

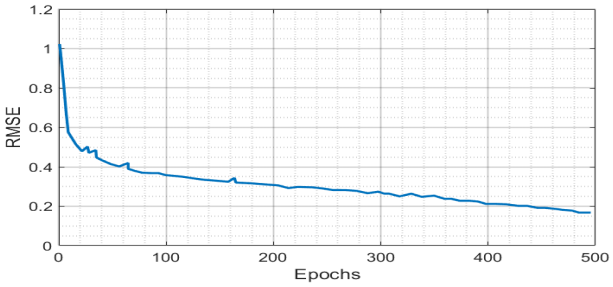

FIGURE 9. RMSE values of the Deep No-reference IQA model during 500 epochs on RSI-CB256.

35 output nodes, corresponding to the number of subclasses in our dataset. This sequence is further enriched by the inclusion of a ReLU activation function. For enhanced robustness and regularization, a dropout layer with a dropout rate of 0.5 is introduced. The model culminates with the application of a LogSoftmax activation function to its output. This model leverages the strengths of the VGG16 architecture, fine-tuning it for the specific needs of multiclass classification in RS and EO data analysis.

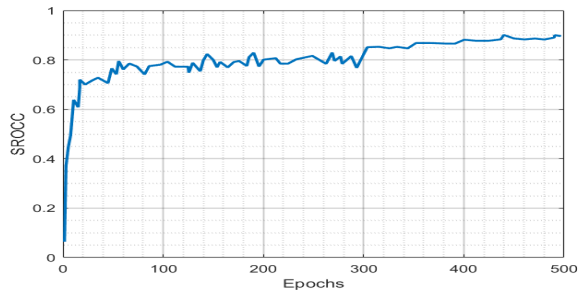

FIGURE 10. SROCC values of the Deep No-reference IQA model during 500 epochs on RSI-CB256.

IV. EXPERIMENTAL RESULTS

In this section, we evaluate the performance of the designed models in the different layers of the proposed AI-driven image management system.

A. NO-REFERENCE DIQA RESULTS

1) EVALUATION METRICS

In order to gauge the model's performance in assessing image quality during the training, testing, and validation steps, some metrics are being introduced for this purpose:

- **SROCC** or "Spearman Rank-Order Correlation Coefficient" [39] measures the strength of monotonicity and correlation between two variables. It ranges from -1 to 1, where 1 indicates perfect correlation, -1 denotes negative monotonicity, and 0 signifies no monotonicity. The formula for SROCC is:

$$SROCC = \rho = 1 - \frac{6\sum \Delta^2}{n(n^2-1)}, \tag{10}$$

  where n is n is the number of images and Δ is the difference between the predicted score and the AMOS of the tested image.
- **KROCC** refers to the "Kendall Rank-Order Correlation Coefficient" [40], similar to SROCC, it assesses the strength and direction of ordinal association between two datasets. With values ranging from -1 to 1, 1 indicates a perfect positive ordinal association, -1 denotes a perfect negative correlation, and 0 signifies no ordinal association. The formula for KROCC is given by:

$$KROCC = \tau = \frac{2(n_c - n_d)}{n(n-1)}, \tag{11}$$

  where n_c is the number of concordant pairs, n_d is the number of discordant pairs, and $\frac{2}{n(n-1)}$ is the total number of pairwise comparisons.
- **PLCC** refers to the "Pearson Linear Correlation Coefficient" [41], a statistical measure assessing the direction of a linear relationship between two sets of variables. Similar to SROCC, the PLCC value ranges from -1 to 1. A value of 1 indicates a perfect positive linear correlation, -1 denotes a negative monotonic

TABLE 3. Performance comparison between the evaluation metrics of our no-reference deep IQA Model and some traditional FR-IQA measures on RSI-CB256.

Evaluation Metrics	NoR-DIQA	FSIM	SSIM	VIF
MAE	**0.165**	0.312	0.334	0.322
RMSE	**0.301**	0.559	0.579	0.562
SROCC	**0.960**	0.937	0.895	0.915
PLCC	**0.995**	0.965	0.922	0.948
KROCC	**0.865**	0.835	0.815	0.825

relationship, and 0 signifies no monotonicity. The formula for PLCC is given by:

$$PLCC = \rho = \frac{\sum((x_i - \mu_x)(y_i - \mu_y))}{\sigma_x \sigma_y}, \quad (12)$$

where μ_x is the mean of x, μ_y is the mean of y, σ_x is the standard deviation of x, σ_y is the standard deviation of y, and $x_i and y_i$ are individual data points from the x and y datasets, respectively.

- **MAE** stands for "mean absolute error," [42] a metric used to evaluate the accuracy of a predictive model. The formula for MAE is given by the following equation:

$$MAE = \frac{\sum |y_i - \bar{y_i}|}{n}, \quad (13)$$

- **RMSE:** stands for "Root Mean Squared Error," [43] a metric that quantifies the average error between predicted and observed values. The RMSE formula is given by the following equation:

$$RMSE = \sqrt{MSE}, \quad (14)$$

where y_i observed values, $\bar{y_i}$ the predicted value of y, and n is the number of data points.

We report results obtained from 500 train-test iterations, where in each iteration, we randomly select 0.8 of the RSI-CB distorted images and their corresponding AMOS as the training set, 0.1 as the validation set, and the remaining 0.1 as the test set.

In Figure 8, the trend of the training loss function for the NoR-DIQA model is shown over 1.2 million training iterations, equivalent to 500 training epochs. The figure demonstrates a consistent decrease in the training loss function throughout each epoch, stabilizing between 700,000 and 1,100,000 iterations. It reaches its minimum value of 0.1 by the conclusion of the training as presented in the formula (2). This trend indicates that the model is trained and able to detect low-quality/distorted images. These results are confirmed in Figures 9 and 10, which show a consistent decrease and increase in the RMSE and SROCC values over 500 training epochs. These curves stabilize from epoch number 400, reaching final values of 0.18 and 0.92, respectively.

Furthermore, the findings presented in Table 3 provide a comprehensive assessment of the proposed model for different evaluation metrics during the testing phase. A performance comparison between our NoR-DIQA model and traditional FR-IQA models (e.g., FSIM, SSIM, and VIF) on the RSI-CB256 dataset reveals compelling statistical insights. A noteworthy MAE value of 0.165, coupled with an RMSE value of 0.301, attests to the model's efficiency in generating accurate predictions of the AMOS. These low error values imply minimal disparity between predicted quality and the input MOS within the 0-10 range. Additionally, the SROCC index of 0.960, the PLCC index of 0.995, and the KROCC index of 0.865 demonstrate a robust positive linear correlation between predicted quality and AMOS. These results affirm the model's strong predictive capabilities, demonstrating high correlation and accuracy. They also highlight the superiority of the proposed solution over traditional IQA techniques. Importantly, the choice to employ a CNN in IQA with RSI is validated, highlighting its inherent ability to extract features from challenging RSI images, a task particularly demanding compared to natural images. CNN's adaptability and feature extraction capabilities underscore its effectiveness in handling the complexities of remote sensing IQA.

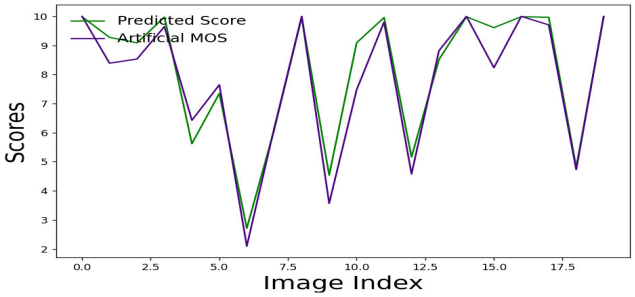

FIGURE 11. Predicted quality scores of the distorted RSI-CB256 testing images with their corresponding AMOS.

Computational speed of NoR-DIQA: The overall processing time for our NoR-DIQA model on these test examples is approximately 0.802 seconds for every set of 10 images, translating to an efficient 0.0802 seconds per individual image. This performance is achieved using a single CPU processor.

To provide a more detailed assessment of our model's performance, Figure 11 shows examples of the predicted AMOS score and the ground-truth score for selected images from the dataset. It shows strong correspondence between the AMOS and the predicted image quality score.

B. LAYER 2: REDUNDANCY REMOVAL RESULTS

In this section, we present the results of the redundancy removal model experiment using a PH method described in Section III-B. Figure 12 illustrates the impact of the Hamming distance threshold on redundancy detection performance in terms of classification accuracy and F1-score. For a threshold increase from 5 to 7, we notice that the accuracy remains relatively stable (around 94%), while the

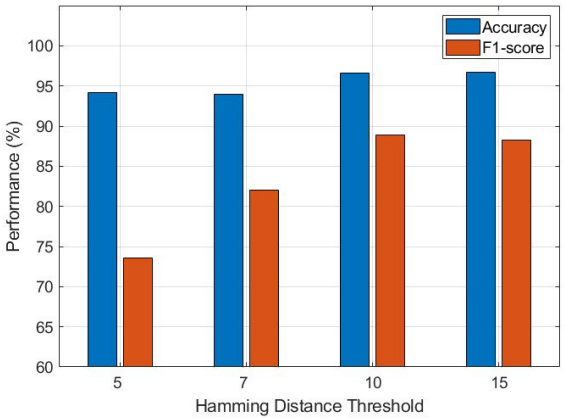

FIGURE 12. Performance of Layer 2 in terms of Accuracy and F1-Score for different Hamming distance thresholds.

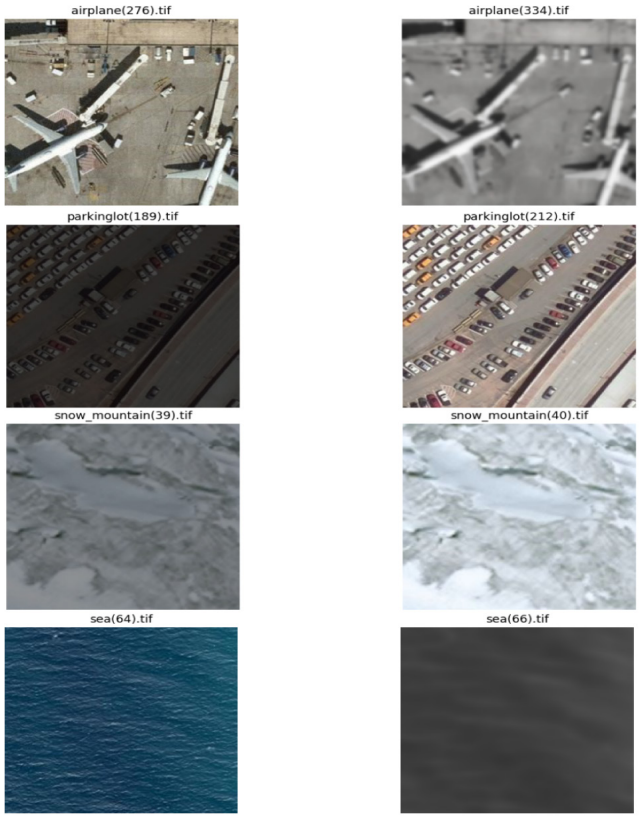

FIGURE 13. RSI-CB256 redundant images with varying distortion levels (blurring and atmospheric noise), representative of real-world distortions experienced by LEO satellite images, were identified using the Perceptual Hashing Algorithm. For example, a Hamming Distance of 10 was used.

F1-score improves noticeably, indicating better identification of redundant samples without excessive removal of relevant data. When the threshold is further increased to 10, both accuracy (96.58%) and F1-score (88.88%) reach their peak values. A further increase to 15 results in only marginal improvement in accuracy (96.70%) but a slight decrease in F1-score (88.25%). Based on these results, a threshold of 10 provides the most balanced and robust performance within the proposed cascaded framework. Finally, in Figure 13, we illustrate examples of the adopted PH algorithm in effectively detecting image redundancy among various classes of LEO satellite RS and EO images, although the presence of multiple distortions with different levels.

TABLE 4. Performance of the DCNN classification model of RS and EO applications.

Metrics	Wide ResNet-50-2	VGG-16
Training Loss	**0.0498**	0.0870
Training Accuracy	**0.9888**	0.9786
Validation Loss	**0.0586**	0.1072
Validation Accuracy	**0.9863**	0.9746
Testing Loss	**0.0496**	0.0974
Testing Accuracy	**0.9941**	0.9687

C. LAYER 3: IMAGE CLASSIFIER RESULTS

Following training and testing in the RSI-CB256 dataset for 20 epochs with a learning rate of 0.0001 using the ADAM optimizer, this section provides a comparative analysis of the classification performance between two selected models for EO image classification: Wide ResNet-50-2 and VGG16. The final results are shown in Table 4, showcasing the training and validation performances of the investigated pre-trained deep CNN models. These results clearly demonstrate effective classification performance among 35 categories of EO applications, robust generalization capabilities, and profound learning aptitude achieved by ResNEt-50-2, which has achieved 0.9941 accuracy compared to 0.9687 for the VGG-16. The remarkable performance of these models underscores their suitability for real-world applications, where high-quality classification and reliable generalization are imperative.

D. PIPELINE TESTING ON SELECTED DATASET CATEGORIES

To further evaluate the effectiveness of the proposed three-layer filtering framework, we select a representative subset of six classes with the largest image subsets in the RSI-CB256 that exhibit diverse textural and spectral characteristics: *shrubwood*, *dry_farm*, *storage_room*, *snow_mountain*, *sparse_forest*, and *desert*. These categories are chosen to encompass various land cover types, including vegetation-rich, arid, and man-made regions, thereby enabling a comprehensive assessment of the model's robustness across heterogeneous visual conditions. An auxiliary *other_objects* class containing irrelevant images. For each class, all samples were originally fit for use. These images are then passed sequentially through the three filtering layers. At each stage, we count how many images are rejected and how many continue to the next layer to calculate the percentage of eliminations per layer and the final proportion of images correctly retained, lost, or incorrectly maintained (intrusions).

TABLE 5. Unified summary of eliminations per layer and final performance statistics.

Class	Input	Layer 1 Elimination (%)	Layer 2 Elimination (%)	Layer 3 Elimination (%)	Correct Matching (%)	Data Loss (%)	Unwanted Data (%)
desert	1092	1.28	4.58	0.37	93.77	6.23	-
dry_farm	1309	5.81	0.23	0.69	93.28	6.72	-
shrubwood	1331	8.70	14.34	0.53	76.41	23.59	-
snow_mountain	1153	6.07	2.17	1.04	90.72	9.28	-
sparse_forest	1110	1.17	9.46	3.69	95.86	4.14	-
storage_room	1307	1.22	15.09	0.46	83.24	16.76	-
other_objects	1115	-	-	-	–	–	0.36
Average (6 subclasses)	**–**	**4.04**	**7.98**	**1.13**	**88.21**	**11.79**	**–**

TABLE 6. Complexity analysis of the proposed three-layer filtering framework with processing time statistics (measured or estimated over 1000 runs).

Layer	Parameters	Memory (FP32)	Processing Time (ms/image)
NoR-DIQA (CNN)	≈0.67M	≈2.7 MB	Min: 75, Max: 88, Avg: 80, Std: 3
Redundancy (pHash)	–	negligible	Min: 1, Max: 3, Avg: 2, Std: 0.5
Classification (Wide ResNet-50-2)	≈68M + 0.53M (head)	∼272 MB (FP32), ≈68 MB (INT8)	Min: 550, Max: 700, Avg: 620, Std: 40

The results presented in Table 5 reveal several important insights about the pipeline's behavior. On average across the six classes, only 4.04% of images were removed by the quality assessment layer, while the redundancy stage accounted for the largest proportion of eliminations (7.98%), reflecting strong visual similarities within several land-cover types. The relevance classifier removed only 1.13% of images, demonstrating the stability and reliability of the Wide ResNet model in preserving valid content. In total, the system correctly retained 88.21% of the fit images while discarding 11.79% as lost data, and the performances vary from one class to another due to the impact of Layer 2. Only 0.36% of irrelevant images from the auxiliary category bypass the full pipeline and are misclassified to one of the desired classes. These results confirm that the proposed framework efficiently identifies and removes low-quality, redundant, and irrelevant samples while preserving the vast majority of useful data. They also confirm the generalization capability of the framework across heterogeneous data, ensuring reliable filtering of low-quality, redundant, and irrelevant satellite imagery while minimizing unnecessary rejection of fit data. The preserved class-wise matching rates (88.21% on average) suggest that mis-filtering at early stages does not significantly propagate or distort downstream performance. While borderline cases may occur, their impact remains limited given the high individual accuracy of each layer.

E. COMPLEXITY ANALYSIS

Table 6 provides a detailed analysis of the complexity of the proposed three-layer filtering framework in terms of parameter count, memory footprint, and processing time. The NoR-DIQA layer is deliberately lightweight, with approximately 0.67M parameters requiring about 2.7 MB of memory, and achieves an average runtime of 80 ms per image on a CPU. The redundancy detection stage, based on perceptual hashing, is non-learned and requires negligible memory, with runtimes consistently below 3 ms per image, showing that this stage has virtually no impact on resource consumption. In contrast, the classification layer, implemented using Wide ResNet-50-2, contains roughly 68M parameters (plus a 0.53M-parameter head), with a memory footprint of about 272 MB in FP32 precision (reduced to 68 MB with INT8 quantization). This layer dominates the computational load, averaging 620 ms per image on CPU, and thus represents the primary bottleneck of the pipeline. These results were obtained on a workstation with an Intel Core i7 CPU (3.6 GHz, 16 GB RAM) without GPU acceleration, which provides a conservative baseline. They suggest that the proposed framework design is compatible with resource-constrained environments, although real-time performance on actual satellite hardware depends on platform-specific characteristics.

F. DISCUSSION AND LIMITATIONS

LEO RS imagery is inherently affected by multiple sources of uncertainty, including cloud coverage, atmospheric disturbances, sensor noise, and variations in illumination and viewing geometry. While the proposed framework does not explicitly model uncertainty in a probabilistic sense, it is designed to implicitly mitigate its impact through a cascaded filtering strategy. Specifically, images with high uncertainty often manifest as low-quality observations and are discarded by Layer 1 of the pipeline. Images that pass this stage but remain irrelevant to the targeted RS or EO application are subsequently removed by the classification layer (Layer 3), further reducing the influence of uncertain or non-informative data. As a result, the pipeline serves as a progressive uncertainty-reduction mechanism by retaining only high-quality, non-redundant, and application-relevant imagery. Nevertheless, limited residual uncertainty

can still propagate across layers, especially in borderline cases. Exploring uncertainty-aware extensions, such as confidence-based filtering or uncertainty-guided mission planning frameworks [44], represents a promising direction for future work.

On the other hand, deploying AI-driven frameworks on-board LEO satellites introduces additional challenges related to limited computational resources, memory capacity, and power budgets. While the experimental results demonstrate that the proposed framework can achieve reasonably fast execution on a general-purpose CPU, these results should be interpreted as a conservative baseline rather than a direct indication of real-time on-board performance. Adapting the framework to resource-constrained space-qualified hardware requires careful optimization, including model compression, quantization, and the selection of lightweight architectures. Nevertheless, the modular design of the proposed three-layer framework facilitates such adaptations, allowing individual components to be optimized or replaced depending on platform capabilities. Investigating and validating these adaptations on representative on-board hardware platforms remains an important direction for future work.

V. CONCLUSION

In this paper, we presented a three-layer filtering framework designed to enhance the efficiency of LEO satellite image transmission by systematically eliminating low-quality, redundant, and non-relevant data. By combining a no-reference image quality assessment model, a perceptual hashing-based redundancy filter, and a deep learning classifier, the framework ensures that only the most valuable imagery is preserved for RS and EO applications. Extensive experiments across multiple datasets confirmed its effectiveness, with each layer outperforming baseline methods—for example, achieving stronger alignment with image quality metrics, robust redundancy detection, and classification accuracy nearing 99.4%. These findings highlight the robustness of the approach in reducing transmission load while improving data utility. Nevertheless, the current evaluation relies on public benchmark datasets and has not yet been validated on real on-board hardware, aspects that are being addressed in our ongoing work. Future research will also investigate adaptive sequencing of the filtering layers, extend the evaluation to additional datasets, and investigate complexity reduction strategies for onboard deployment to enhance the framework's applicability in real satellite operations.

REFERENCES

[1] Y. Li, M. Wang, K. Hwang, Z. Li, and T. Ji, "LEO satellite constellation for global-scale remote sensing with on-orbit cloud AI computing," *IEEE J. Sel. Topics Appl. Earth Observ. Remote Sens.*, vol. 16, pp. 9369–9381, 2023.

[2] T. V. La and C. Messager, "Convective system observations by LEO and GEO satellites in combination," *IEEE J. Sel. Topics Appl. Earth Observ. Remote Sens.*, vol. 14, pp. 11814–11823, 2021.

[3] F.-A. Georgescu, C. Vaduva, D. Raducanu, and M. Datcu, "Feature extraction for patch-based classification of multispectral Earth observation images," *IEEE Geosci. Remote Sens. Lett.*, vol. 13, no. 6, pp. 865–869, Jun. 2016.

[4] A. Bakambekova, N. Kouzayha, and T. Al-Naffouri, "On the interplay of artificial intelligence and space-air-ground integrated networks: A survey," *IEEE Open J. Commun. Soc.*, vol. 5, pp. 4613–4673, 2024.

[5] K. A. M. Abir, B. Dey, M. Redowan, A. Haque, and R. Ahmed, "Predicting suitable habitats for Asian elephant (elephas maximus) in tropical Asia under changing climatic scenarios," *Geography Sustainability*, vol. 6, no. 2, Apr. 2025, Art. no. 100279. [Online]. Available: https://www.sciencedirect.com/science/article/pii/S2666683925000185

[6] A. Cherni, A. Bousselmi, L. Sboui, and Y. Neji, "A hybrid machine learning-deep learning framework for early wheat crop stress detection in Northwest Tunisia under climate change using multi-temporal satellite data," in *Proc. 40th Int. Conf. Adv. Inf. Netw. Appl. (AINA)*, Apr. 2026. [Online]. Available: https://www.dropbox.com/scl/fi/w3ilb1cc4ly90x13nzmrq/C41-AINA-26_AI_Wheat_Aya_Cherni.pdf?rlkey=odylvrwsjqaj1ugggx8l25nws&dl=1

[7] N. Aloui, S. Flores-Mejia, and L. Sboui, "Satellite imagery and AI-based detection of common waterhemp (AMATU) infestation in soybean fields," in *Proc. IEEE Int. Multi-Conf. Smart Syst. Green Process*, Nov. 2025. [Online]. Available: https://www.dropbox.com/scl/fi/d7r12jm00xn4z2cvirrn1/C39-Nourhene_AMATU_AI_Sat_IMC-SSGP-25.pdf?rlkey=my9oqmn8me9ff3uyltzfyit5j&st=wnaf9k6w&dl=1

[8] F. S. Prol, A. Smirnov, S. Kaasalainen, M. M. Hoque, M. Z. H. Bhuiyan, and F. Menzione, "The potential of LEO-PNT mega-constellations for ionospheric 3-D imaging: A simulation study," *IEEE J. Sel. Topics Appl. Earth Observ. Remote Sens.*, vol. 16, pp. 7559–7571, 2023.

[9] C. Serief, Y. Ghelamallah, and Y. Bentoutou, "Deep-learning-based system for change detection onboard Earth observation small satellites," *IEEE J. Sel. Topics Appl. Earth Observ. Remote Sens.*, vol. 16, pp. 8115–8124, 2023.

[10] B. Chintalapati, A. Precht, S. Hanra, R. Laufer, M. Liwicki, and J. Eickhoff, "Opportunities and challenges of on-board AI-based image recognition for small satellite Earth observation missions," *Adv. Space Res.*, vol. 75, no. 9, pp. 6734–6751, May 2025.

[11] P. Bartmiński and M. Siłuch, "Spatial resampling of remote sensing data–accuracy vs. Redundancy," *Polish J. Soil Sci.*, vol. 53, no. 2, pp. 293–306, 2020.

[12] M. P. Uddin, M. A. Mamun, and M. A. Hossain, "PCA-based feature reduction for hyperspectral remote sensing image classification," *IETE Tech. Rev.*, vol. 38, no. 4, pp. 377–396, Jul. 2021.

[13] Z. Zhang, S. Gu, S. Li, Y. Yang, and Q. Zhang, "Multi-hop coflow routing for LEO distributed computation satellite networks," in *Proc. IEEE 96th Veh. Technol. Conf. (VTC-Fall)*, Sep. 2022, pp. 1–5.

[14] A. Ktari, H. Ghazzai, F. Rouissi, L. Sboui, and G. Setti, "Dynamic data routing for non-ISL LEO satellite-based NT-IoT communications," *IEEE Wireless Commun. Lett.*, vol. 15, pp. 760–764, 2026.

[15] A. Hamrouni, H. Ghazzai, G. Setti, and L. Sboui, "LSTM-based dynamic routing with non-ISL LEO satellite constellations for remote IoT connectivity," in *Proc. IEEE Global Commun. Conf.*, Cape Town, South Africa, Dec. 2024, pp. 1473–1478.

[16] C. Wu, Y. Zhu, and F. Wang, "DSFL: Decentralized satellite federated learning for energy-aware LEO constellation computing," in *Proc. IEEE Int. Conf. Satell. Comput. (Satellite)*, Nov. 2022, pp. 25–30.

[17] G. Guerrisi, F. D. Frate, and G. Schiavon, "Artificial intelligence based on-board image compression for the Φ-Sat-2 mission," *IEEE J. Sel. Topics Appl. Earth Observ. Remote Sens.*, vol. 16, pp. 8063–8075, 2023.

[18] N. Longépé, I. Petrelli, N. O. Kadunc, D. Peressutti, R. D. Prete, M. Casaburi, I. Babkina, N. Vercruyssen, E. C. Luis, Á. M. Elorza, V. Marchese, A. P. Kidron, and N. Melega, "Simulation of multispectral and hyperspectral EO products for onboard machine learning application," *IEEE J. Sel. Topics Appl. Earth Observ. Remote Sens.*, vol. 17, pp. 17651–17665, 2024.

[19] N. Ruan, K. Li, Q. Zhang, L. Lovén, P. K. Donta, Y. Jia, and S. Dustdar, "Edge AI for Earth observation," *IEEE Internet Comput.*, vol. 29, no. 3, pp. 31–40, May 2025.

[20] K. Ding, Z. Yang, Y. Wang, and Y. Liu, "An improved perceptual hash algorithm based on U-net for the authentication of high-resolution remote sensing image," *Appl. Sci.*, vol. 9, no. 15, p. 2972, Jul. 2019.

[21] M. Yu, Z. Tang, X. Zhang, B. Zhong, and X. Zhang, "Perceptual hashing with complementary color wavelet transform and compressed sensing for reduced-reference image quality assessment," *IEEE Trans. Circuits Syst. Video Technol.*, vol. 32, no. 11, pp. 7559–7574, Nov. 2022.
[22] H. Li, X. Dou, C. Tao, Z. Wu, J. Chen, J. Peng, M. Deng, and L. Zhao, "RSI-CB: A large-scale remote sensing image classification benchmark using crowdsourced data," *Sensors*, vol. 20, no. 6, p. 1594, Mar. 2020.
[23] G. Rohith and L. S. Kumar, "Remote sensing signature classification of agriculture detection using deep convolution network models," in *Proc. Int. Conf. Mach. Learn.*, 2020, pp. 343–355.
[24] A. Stateczny, S. M. Bolugallu, P. B. Divakarachari, K. Ganesan, and J. R. Muthu, "Multiplicative long short-term memory with improved mayfly optimization for LULC classification," *Remote Sens.*, vol. 14, no. 19, p. 4837, Sep. 2022.
[25] P. P. Tumpa and M. S. Islam, "Lightweight parallel convolutional neural network with SVM classifier for satellite imagery classification," *IEEE Trans. Artif. Intell.*, vol. 5, no. 11, pp. 5676–5688, Nov. 2024.
[26] Q. Wang, H. Ye, D. Liang, and S.-J. Huang, "Diffusion-noise-based augmentation for long-tailed remote sensing image classification," *IEEE Trans. Geosci. Remote Sens.*, vol. 63, 2025, Art. no. 5626114, doi: 10.1109/TGRS.2025.3568812.
[27] A. Alaei, V. Bui, D. Doermann, and U. Pal, "Document image quality assessment: A survey," *ACM Comput. Surv.*, vol. 56, no. 2, pp. 1–36, Feb. 2024.
[28] Y. Al-Najjar and C. Soong, "Comparison of image quality assessment: PSNR, HVS, SSIM, UIQI," *Int. J. Sci. Eng. Res.*, vol. 3, pp. 1–5, Jan. 2012.
[29] K. Ohashi, Y. Nagatani, M. Yoshigoe, K. Iwai, K. Tsuchiya, A. Hino, Y. Kida, A. Yamazaki, and T. Ishida, "Applicability evaluation of full-reference image quality assessment methods for computed tomography images," *J. Digit. Imag.*, vol. 36, no. 6, pp. 2623–2634, Dec. 2023.
[30] J. Yao, J. Shen, and C. Yao, "Image quality assessment based on the perceived structural similarity index of an image," *Math. Biosciences Eng.*, vol. 20, no. 5, pp. 9385–9409, 2023.
[31] L. Zhang, L. Zhang, X. Mou, and D. Zhang, "FSIM: A feature similarity index for image quality assessment," *IEEE Trans. Image Process.*, vol. 20, no. 8, pp. 2378–2386, Aug. 2011.
[32] D. Zhang, Y. Ding, and N. Zheng, "Nature scene statistics approach based on ICA for no-reference image quality assessment," *Proc. Eng.*, vol. 29, pp. 3589–3593, Feb. 2012.
[33] A. C. Grivei, I. C. Neagoe, F. A. Georgescu, A. Griparis, C. Vaduva, Z. Bartalis, and M. Datcu, "Multispectral data analysis for semantic assessment—A SNAP framework for sentinel-2 use case scenarios," *IEEE J. Sel. Topics Appl. Earth Observ. Remote Sens.*, vol. 13, pp. 4429–4442, 2020.
[34] L. S. Chow and H. Rajagopal, "Modified-BRISQUE as no reference image quality assessment for structural MR images," *Magn. Reson. Imag.*, vol. 43, pp. 74–87, Nov. 2017.
[35] D. Marmanis, M. Datcu, T. Esch, and U. Stilla, "Deep learning Earth observation classification using ImageNet pretrained networks," *IEEE Geosci. Remote Sens. Lett.*, vol. 13, no. 1, pp. 105–109, Jan. 2016.
[36] B. Dey, M. Masum Ul Haque, R. Khatun, and R. Ahmed, "Comparative performance of four CNN-based deep learning variants in detecting hispa pest, two fungal diseases, and NPK deficiency symptoms of Rice (Oryza sativa)," *Comput. Electron. Agricult.*, vol. 202, Nov. 2022, Art. no. 107340. [Online]. Available: https://www.sciencedirect.com/science/article/pii/S0168169922006494
[37] K. He, X. Zhang, S. Ren, and J. Sun, "Deep residual learning for image recognition," 2015, *arXiv:1512.03385*.
[38] S. Liu and W. Deng, "Very deep convolutional neural network based image classification using small training sample size," in *Proc. 3rd IAPR Asian Conf. Pattern Recognit. (ACPR)*, Nov. 2015, pp. 730–734.
[39] R. N. Forthofer, E. S. Lee, and M. Hernandez, "3-descriptive methods," in *Biostatistics*, 2nd ed., New York, NY, USA: Academic, 2007, pp. 21–69.
[40] W. W. Daniel, "Kendall's tau," in *Applied Nonparametric Statistics*, 2nd ed. Boston, MA, USA: PWS-Kent, 1990, pp. 365–377.
[41] H. Liu, "Description methods of spatial wind along railways," in *Wind Forecasting in Railway Engineering*, 2021, pp. 251–282.
[42] Y.-H. Kiang, "Chapter 2-model development and validation methodology: A classical big data application," in *Fuel Property Estimation and Combustion Process Characterization*. New York, NY, USA: Academic, 2018, ch. 2, pp. 11–39.
[43] A. Mason, J. Rioux, S. E. Clarke, A. Costa, M. Schmidt, V. Keough, T. Huynh, and S. Beyea, "Comparison of objective image quality metrics to expert Radiologists' scoring of diagnostic quality of MR images," *IEEE Trans. Med. Imag.*, vol. 39, no. 4, pp. 1064–1072, Apr. 2020.
[44] X. Li and Y. Dong, "A value-guided mission planning framework for Earth observation satellites under uncertainty in digital twins," *Measurement*, vol. 259, Feb. 2026, Art. no. 119686.

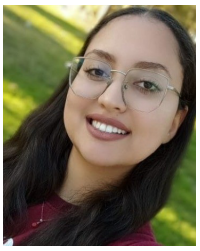

NOURHEN SBOUI (Student Member, IEEE) received the degree in information and communication technologies (ICT) engineering from the École Supérieure des Communications de Tunis (SUP'COM), University of Carthage, in 2024. She is currently pursuing the Ph.D. degree in ICT engineering with the XLIM Laboratory, Poitiers University, France. She worked as a Research Consultant in collaboration with Abu Dhabi University. Her research interests include autonomous vehicles, low-earth orbit (LEO) satellites, 5G resource allocation, and industry 4.0.

HAKIM GHAZZAI (Senior Member, IEEE) received the Diplôme d'Ingénieur degree (Hons.) in telecommunication engineering and the master's degree in high-rate transmission systems from the École Supérieure des Communications de Tunis (SUP'COM), Tunis, Tunisia, in 2010 and 2011, respectively, and the Ph.D. degree in electrical engineering from the King Abdullah University of Science and Technology (KAUST), Saudi Arabia, in 2015. He was a Research Scholar with Qatar Mobility Innovations Center (QMIC), Qatar; Karlstad University, Sweden; and the Stevens Institute of Technology, NJ, USA. He is currently a Senior Research Scientist with KAUST. He is the author and co-author of more than 200 publications. His research interests include artificial intelligence-enabled applications, the Internet of Things, intelligent transportation systems (ITS), and mobile and wireless networks.

SAMEH NAJEH (Member, IEEE) received the Ph.D. degree in telecommunications from the National Engineering School of Tunis (ENIT), Tunisia, in 2008, and the Habilitation to lead research (HDR) degree in telecommunications from the Higher School of Communication of Tunis (Sup'Com), in 2020. She is currently an Associate Professor of signal processing and telecommunications with Sup'Com, University of Carthage. Her research interests include signal processing and digital communication. Her current research interests include radio resource management in 6G and beyond based on game theory, IA, graph theory tools for various applications, advancing smart city applications, empowered robotics, and undersea communication.

LOKMAN SBOUI (Senior Member, IEEE) received the Diplôme d'Ingénieur degree (Hons.) from the École Polytechnique de Tunisie (EPT), La Marsa, Tunisia, in 2011, and the M.Sc. and Ph.D. degrees from the King Abdullah University of Science and Technology (KAUST), in 2013 and 2017, respectively. He is currently an Associate Professor with the Department of System Engineering, École de Technologie Supérieure (ÉTS), Montreal, Canada. His research interests include energy-efficient wireless communications, LEO satellites for the IoT, automation, urban air mobility (UAM), edge computer vision, and cognitive radio. He has been on the editorial board of IEEE Wireless Communications Letters since 2021.